APPLICATIONS OF MULTIZONE EULER/NAVIER-STOKES AERODYNAMIC METHODS TO AIRCRAFT CONFIGURATIONS

P. Raj*, C. R. Olling**, and S. W. Singer***
Lockheed Aeronautical Systems Company
Burbank, CA 91520-7551

Abstract

Computational methods based on cell-centered finite-volume spatial discretization and explicit time-stepping algorithm for solving the Euler and Navier-Stokes equations are used to simulate inviscid and viscous flow about configurations ranging from simple two-dimensional airfoils to complete aircraft. Solutions are obtained using patched multizone grids with matching and different grid densities across zonal interfaces. Emphasis is placed on evaluating the sensitivity of computed solutions to numerical dissipation associated with the cell-centered finite-volume schemes, and the effects of grid density and turbulence modeling. This is accomplished by correlating computed solutions with experimental data and analytical solutions, wherever possible. The results provide an added measure of confidence in the computational solutions of the Euler and Navier-Stokes equations, and also point out some of the limitations.

I. Introduction

One of the factors contributing to high cost of aircraft development is the need to evaluate numerous geometrical modifications to ensure that the final design will meet all mission requirements while maintaining desired levels of performance. For the aerodynamic part of the design, such evaluations are most effectively performed by a combination of wind-tunnel testing and computational simulations. The wind-tunnel testing offers a reliable and proven means of predicting aerodynamic data, but it can be expensive and time consuming, especially when surface and flow-field measurements are made, due to model fabrication, labor, and energy requirements. The costs are even higher when tests are conducted to minimize scale effects and wall interference. For some flight regimes, wind tunnel testing is not feasible at all. Computational simulations promise to alleviate precisely these kinds of deficiencies.

Methods for computational aerodynamic analysis have made significant progress over the past two decades. The boundary integral methods, popularly known as panel methods [1-4], were the first to be developed. They are now widely used in various phases of aircraft design but their application is restricted to purely subsonic or supersonic flows due to the inherent limitations of their linearized potential flow formulation. For transonic flows, nonlinear potential flow methods based on transonic small-disturbance equations [5] and full-potential equations [6,7] have been developed. However, accuracy of their solutions deteriorates in the presence of strong shocks or rotational flows. These limitations of the potential-flow codes can be alleviated by solving the Euler equations, which allow nonisentropic shocks and rotational flows to be a part of the solution [8,9]. However, the precise structure of the shocks and rotational flows cannot be modeled accurately without solving the Navier-Stokes equations. Also, the Euler solutions cannot adequately model flows dominated by viscous effects.

The Navier-Stokes equations adequately model the physics of a large class of flow phenomena for which continuum is a valid assumption. (The Boltzmann equations based on the kinetic theory of gases need to be solved for modeling molecular flows.) Solving the Navier-Stokes equations to simulate laminar flows is quite common, but using these equations to model even simple turbulent flows stretches the current supercomputers to their limits [10]. At present, the Reynolds-averaged Navier-Stokes (RANS) equations are used almost exclusively to simulate complex turbulent flows typically encountered by flight vehicles.

The RANS methods are capable of analyzing a variety of configurations ranging from two-dimensional (2-D) airfoils [11] to three-dimensional (3-D) configurations including complete aircraft [12-14]. Their effective use in the design environment is largely hampered by three factors: (1) they require relatively large amounts of computational storage and time; (2) generating suitable grids for complex configurations is tedious and time consuming; and (3) accuracy of computed solutions is subject to inadequacies of turbulence modeling and numerical parameters such as grid density, numerical dissipation, etc. Improved algorithms and increased speed and memory of supercomputers promise to alleviate the first difficulty. Significant progress is also being made in improving the grid generation process [15,16]. However, turbulence model inadequacies persist [11,17] for complex flows typified by shock-induced separation and vortical flows. Also, sensitivity of the solutions to variations in numerical parameters is not fully documented.

In this paper, computed solutions are presented for five test cases to illustrate the capabilities and limitations of two methods, namely, the Three-dimensional Euler/Navier-Stokes Aerodynamic Method (TEAM) and the Three-dimensional Reynolds-Averaged Navier-Stokes Aerodynamic Method (TRANSAM). Special attention is given to evaluating the sensitivity of solutions to grid density, numerical dissipation, and turbulence models. The TEAM code [18] has been developed by Lockheed under a U.S. Air Force contract. The TRANSAM code is an extension of the TEAM code and it serves primarily as a testbed for turbulence models. Computed solutions for the test cases are compared with available analytical, numerical, and experimental data. The remainder of the paper is divided into two major sections followed by concluding remarks. Basic features of

* R&D Engineer, Aerodynamics Department
** Research Specialist, Aerodynamics Department
*** Aerodynamicist, Aerodynamics Department

the TEAM and TRANSAM codes are highlighted in Section II and the analysis results are discussed in Section III.

II. Basic Features of TEAM and TRANSAM

The TEAM and TRANSAM codes are designed to compute steady-state solutions of the Euler, RANS, and Navier-Stokes equations representing conservation of mass, momentum, and energy, expressed in unsteady, integral form. The computational algorithm employs finite-volume spatial discretization, proposed by Jameson et al. [19], producing a set of ordinary differential equations which are integrated in time using a multistage time-stepping procedure. The finite-volume formulation requires that the region surrounding a given configuration be divided into an ordered set of hexahedral cells. Such a set, called a grid or a mesh, may be constructed in any convenient manner; only the Cartesian coordinates of the cell vertices are required to carry out the solution process. The basic features of the codes are highlighted here; other details can be found in References 9, 13, and 18.

Multiple Zones.-- Both codes can accommodate patched zonal grids of arbitrary topologies. Across zonal interfaces, three classes of grid distributions, shown in Figure 1, are allowed, namely,

Class 1: One-to-one nodal point matching.
Class 2: Nodal points of one grid being an ordered subset of the other grid.
Class 3: Mismatched nodal point distributions.

Every cell at the zonal boundary has an image cell associated with it. Note that the image cells do not physically exist; they are fabricated to facilitate computation of fluxes for all faces--interior as well as boundary--using the same formulation.

Multizone architecture is particularly useful for analyzing complex configurations since it allows considerable flexibility in grid generation. It also permits efficient modeling of viscous effects because the RANS equations need to be solved only in selected regions of the flow field; the Euler equations are solved elsewhere. In addition, Class 2 and 3 type interfaces can be utilized to improve accuracy and/or computational efficiency. These aspects are further discussed in the Results section.

Turbulence Models.-- The well-known Baldwin-Lomax turbulence model [20] is included in the TEAM code. Three additional models have been incorporated into TRANSAM and their effectiveness is being evaluated. These models are: renormalization group (RNG) theory based algebraic model [21]; Johnson-King model [22]; and Chien two-equation model [23]. The corresponding solutions for an airfoil are included in this paper.

The Baldwin-Lomax model is an algebraic two-layer model widely used for computing attached and mildly separated turbulent flows. It is an equilibrium model that does not include turbulence history effects. The eddy viscosity is not related to boundary-layer thickness or displacement thickness. Instead, a maximum of a function $f = \rho n \omega$ is located in the direction normal to the solid surface to estimate eddy viscosity. Here, n is the normal distance from the solid surface and ω is the vorticity magnitude. In some cases, there can be multiple maxima of f. Degani and Schiff [24] proposed a scheme for choosing the correct maximum of f in cases where a basically inviscid vortex is present outside the boundary layer.

The RNG algebraic model, included in TRANSAM, is also an equilibrium model. It relies upon the systematic elimination of small-scale turbulent fluctuations using renormalization group theory. The theory determines both the mathematical model and the values of the model constants. A length-scale must still be specified, which leads to some loss of generality of the model. In the present form this length-scale is postulated from physical considerations for boundary-layer flows. Also, it is assumed that the rate of dissipation of turbulent kinetic energy is equal to the rate of production of turbulent kinetic energy. A cubic equation is solved to determine the eddy viscosity.

The Johnson-King model makes use of an additional differential equation representing the maximum turbulent shear stress for boundary-layer flows. It is a nonequilibrium model that includes turbulence history effects. This model was developed specifically to improve the accuracy of separated flow simulations. Predictions of attached

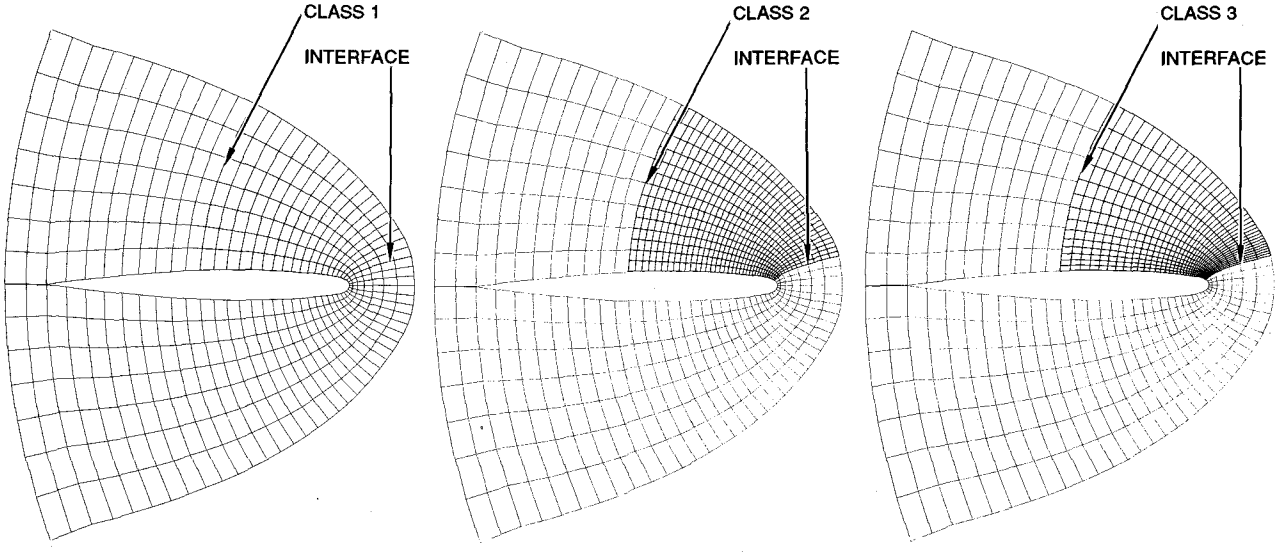

Fig. 1 Three classes of zonal interfaces of multizone grids

flows in adverse pressure gradients have sometimes been reported to be inferior to predictions based on algebraic turbulence models, such as the Baldwin-Lomax model. Recently, a modification to the Johnson-King model has been proposed by Abid and Johnson [25] that improves this situation.

The Chien two-equation model solves two additional partial differential equations for turbulent kinetic energy, k, and rate of dissipation, ε. It is a nonequilibrium model and therefore includes turbulence history effects. A difference from the other models in TRANSAM is that a length-scale is not algebraically specified but computed using k and ε, and thereby increasing the generality of the model. At a solid boundary, k and ε are set to zero. This is a low-Reynolds number model in which the integration is carried out all the way to the solid surface that can lead to "stiff" equations requiring a smaller time step. Another drawback is the necessity of specifying initial conditions for k and ε.

Spatial Discretization.-- In the cell-centered finite-volume formulation used to discretize the spatial terms, the flow variables are defined at cell centers and fluxes are computed at cell faces. A simple arithmetic average of the cell-center values in two neighboring cells is used to estimate the convective and viscous fluxes, as well as flow variables, at the faces. The flow gradients required to estimate the viscous fluxes are computed using either the divergence-theorem approach of Jayaram and Jameson [26] or chain-rule differentiation.

This discretization is equivalent to a central-difference approximation which is second-order accurate on smooth grids. For Euler equations, the resulting semi-discrete equations have to be augmented by numerical dissipation terms (also known as artificial or numerical viscosity) in order to prevent instabilities arising from aliasing error due to high-frequency error components, to suppress odd-even decoupling, to capture shocks, and to minimize oscillations in regions of high gradients. These terms are needed even when solving the RANS equations because the viscous dissipation is generally not sufficient to suppress the high-frequency error. In TEAM and TRANSAM, two types of schemes, namely, adaptive and characteristic-based, are used to construct the dissipation terms.

Adaptive Dissipation.-- The adaptive dissipation schemes employ differences of the flow variables directly. Two types of schemes are included in the codes: (1) standard and modified adaptive dissipation (SAD and MAD); and (2) flux-limited adaptive dissipation (FAD). The SAD scheme uses blended first and third differences as proposed by Jameson et al. [19]. The MAD schemes are derived from SAD by selecting different scaling factors for the difference terms to reduce the overall level of dissipation. The reduction is particularly desirable for viscous computations in order to prevent the numerical dissipation from overwhelming the viscous dissipation. The FAD scheme employs only third differences with appropriate flux limiters [27]; the first-difference terms are not used. For a scalar conservation law, it becomes a total variation diminishing (TVD) scheme provided that the coefficients are appropriately chosen. The FAD scheme is capable of nonoscillatory shock capture. The mathematical formulation of these schemes is given in Appendix A.

Near the boundaries of the computational region, the dissipation terms have to be constructed differently than those for the interior since the present algorithm uses only one image cell. Three options for defining the dissipation terms are outlined in Appendix A. For multizone grids, the use of Option 1 at zonal interfaces resulted in divergence of the solution process which could be remedied by using Options 2 or 3. Option 3 is formally the least dissipative and it has been used to obtain most of the solutions reported in this paper.

All schemes use two user-specified parameters, VIS-2 and VIS-4, to control the level of dissipation. For the SAD and MAD schemes, the input VIS-4 parameter (divided internally by 64) scales the third-difference terms and controls the background dissipation needed to suppress high-frequency error components whereas the VIS-2 parameter is used to minimize wiggles and overshoots near shocks and stagnation points. For the FAD scheme, the value of VIS-4 determines a lower bound on dissipation and VIS-2 may be adjusted to ensure that there is enough dissipation to eliminate oscillations near shocks.

Characteristic-based Dissipation.-- Although the adaptive dissipation schemes are quite effective, difficulties may be encountered in simulating high-speed flows because these schemes do not accurately model the wave propagation in supersonic flows. The characteristic-based schemes (also known as upwind schemes) provide appropriate upwind bias for supersonic flows albeit at the expense of additional computations compared to the adaptive schemes. In TEAM and TRANSAM, the symmetric TVD formulation with Roe averaging described by Gnoffo et al. [28] is used. In its simplest form, this formulation leads to a first-order accurate upwind scheme. A second-order accurate upwind scheme results from using a flux limiter. Both options are included in the codes and the user can select either one by changing the value of an input parameter. The input value of the VIS-2 parameter serves as an eigenvalue limiter near the critical points; i.e., stagnation points, sonic points, and shocks. The input value of VIS-4 is used to scale the dissipative terms to provide enhanced stability.

Boundary Conditions.-- Appropriate nonreflecting boundary conditions based on Riemann invariants are used at the far-field boundaries. For inviscid Euler computations, a no-normal-flow condition is imposed on the solid surface and the value of pressure on the surface is estimated using the normal momentum equation as described in Reference 18. For viscous computations, the no-slip condition is applied at solid surfaces which are also assumed to be adiabatic. If needed, a constant temperature condition can be prescribed. At a nacelle inflow or inlet face, Mach number, pressure ratio, speed ratio, or mass-flow ratio (MFR) can be specified. At the exhaust face, nozzle pressure ratio (NPR), total temperature ratio, and exit flow direction need to be prescribed. At a zonal interface along which two zones are patched, the flux-conserving boundary conditions are used [18].

Time Marching.-- The set of ordinary differential equations resulting from the finite-volume spatial discretization is integrated in time using a multistage time-stepping scheme with options for three, four, or five stages. Convergence to a steady state is typically achieved in hundreds of time steps, rather than thousands typically

required by a more conventional explicit scheme using a global minimum-step size, because the use of local time step (i.e., a different step size for each cell determined solely by the local stability restrictions) is augmented by enthalpy damping (for inviscid flows) and implicit residual smoothing.

Analysis Process.-- The analysis starts with the flow variables, namely, density, three Cartesian components of momentum, and total energy, in all cells initialized to free-stream conditions. This is equivalent to an impulsive start. Following each time step, the ratio of the current and the initial values of the average residual (root-mean-square value of the net mass flux) is checked to determine whether a steady state has been reached. The time marching stops if a pre-specified convergence criterion is met or after a prescribed number of steps. The code has a provision to restart the solution process and perform additional steps if needed.

III. Results and Discussion

In this section, solutions are presented for five test cases, namely, NLR 7301 airfoil, RAE 2822 airfoil, Lockheed-AFOSR Wing C, a canard-wing-body, and the advanced nozzle concept (ANC) fighter configuration. In all cases, the flow was impulsively started and no Kutta condition was explicitly applied; shocks and rotational-flow regions were automatically captured. At least a four orders of magnitude reduction in the average residual was used as a convergence criterion. In many cases, the time marching was advanced even further to examine any changes. All 3-D cases considered here involve symmetrical flight conditions. Therefore, only half the configuration was analyzed.

NLR 7301 Airfoil.-- Analysis of this airfoil was primarily motivated by the availability of a shockfree transonic solution of the Euler equations, obtained using the hodograph technique [29], which could be used to evaluate the accuracy of the TEAM computations. The solution corresponds to a free-stream Mach number (M_∞) of 0.721 and an angle of attack (α) of -0.194^o. For these conditions, TEAM analysis was performed using several O-type grids with the coarsest having 2,025 nodes and the finest having 103,041. For all cases, the far-field boundary was located nearly 80-chords away based on the results of a previous study [30] where the effect of the far-field boundary location was investigated. No far-field vortex correction was used because its effect on the results was found to be negligible when the outer boundary was moved past 60 chords.

Sensitivity of the solutions to numerical dissipation schemes and grid density was partially addressed by Raj [9]. For most grids but the coarser ones (less than 25,000 nodes), the computed surface-pressure and Mach-number distributions were found to agree well with the hodograph solution except in the aft region of transition from supersonic to subsonic flow. The computed solutions there exhibited a wiggle whose amplitude varied with the grid distribution. The amplitude of the wiggle increased as the number of points on the O curves increased from 161 to 241 to 321 while holding the number of O curves fixed at 49. On the other hand, the amplitude decreased as the number of O curves increased from 33 to 49 to 65 to 81 while keeping the number of points on each curve fixed at 241.

To investigate the effect of grid density and numerical dissipation further, grids with 81 x 321, 161 x 321, and 321 x 321 nodes were selected. The lift and pitching moment coefficients exhibited relatively little sensitivity to grids and dissipation. The computed value for lift was nominally 0.5959 which compares favorably with the "exact" solution (numerical integration of hodograph data) of 0.5949 and the hodograph prediction of 0.5939. The computed pitching moment of -0.1325 compares well with -0.1298 given as the exact solution. Sensitivity of the drag coefficient (exact solution being 0.0005 and hodograph prediction being 0.0) is shown in Table 1. The results confirm the low levels of dissipation for the the MAD-2 scheme.

Table 1 Drag Sensitivity to Grid Density for NLR 7301 Airfoil, $M_\infty = 0.721$, $\alpha = -0.194^o$

	49 x 321	81 x 321	161 x 321	321 x 321
SAD	0.000577	0.000294	0.00025	0.00027
MAD-1	0.000464	0.000282	0.000241	0.000241
MAD-2	0.000354	0.000245	0.000206	0.000207
FAD	0.000804	0.000505	0.000394	0.000367

The computed surface pressure distribution on the 81 x 321, 161 x 321, and 321 x 321 grids compared well with each other and the hodograph solution. A typical comparison for the finest grid (321 x 321) is shown in Figure 2(a). The total-pressure loss distribution on the surface is shown in Figure 2(b). On a large part of the airfoil, the total pressure losses are less than a 1/4-percent. Ideally, they should be zero.

RAE 2822 Airfoil.-- The RAE 2822 airfoil has been experimentally tested by Cook et al. [31] and has become a standard test case for evaluating viscous computational methods [11]. Solutions for two flow conditions corresponding to Case 6 and Case 10 are presented here.

Case 6 TEAM computations were performed at $M_\infty = 0.725$, $\alpha = 2.4^o$ (corrected) and Reynolds number based on chord, Re_c, of 6.5 million. Thin-layer RANS solutions were obtained on two C grids, a 64 x 161 coarse grid (161 nodes in the wrap around direction and 64 in the normal direction with appropriate clustering to resolve the boundary layer), and a 129 x 257 fine grid. The coarse grid was divided into an inner and an outer zone. Solving RANS equations in the inner zone, and either RANS or Euler in the outer zone produced identical solutions. Of course, the use of Euler equations reduced overall computational time. The fine grid was divided into six zones and RANS equations were solved in all zones. The Baldwin-Lomax turbulence model was used for all viscous solutions, and the flow was considered to be turbulent on the entire airfoil.

The computed solutions are compared with each other and with the experimental data in Table 2 and Figure 3. An Euler solution on a 64 x 161 grid is also included for the sake of completeness. Viscous solutions on the finer grid clearly show a better agreement with the measured data. The illustration also demonstrates relatively little sensitivity to using MAD-1 or MAD-2 scheme. However, the use of MAD-1 improved robustness and convergence rate.

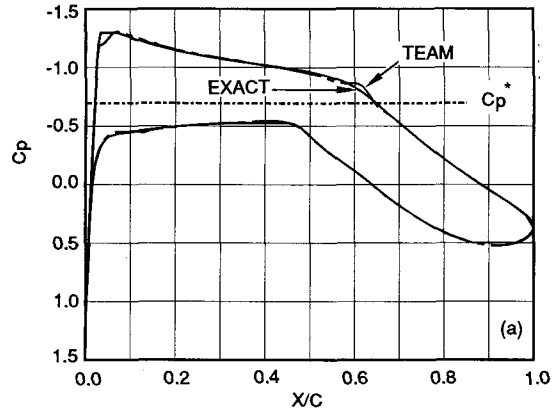

Fig. 2(a) Correlation of computed (TEAM) and exact (hodograph) surface pressure distribution for NLR 7301, $M_\infty = 0.721$, $\alpha = -0.194^o$

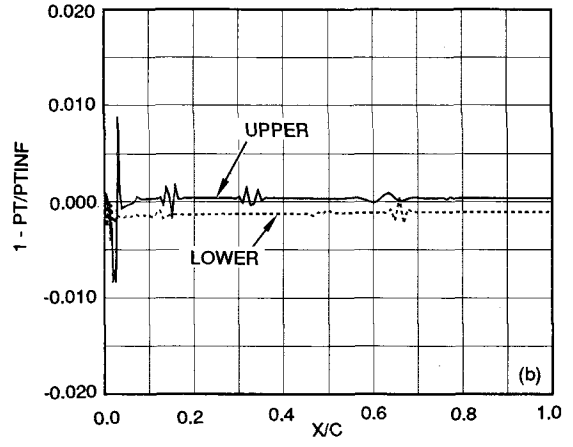

Fig. 2(b) Surface total pressure loss distribution, TEAM computation for NLR 7301 airfoil, $M_\infty = 0.721$, $\alpha = -0.194^o$

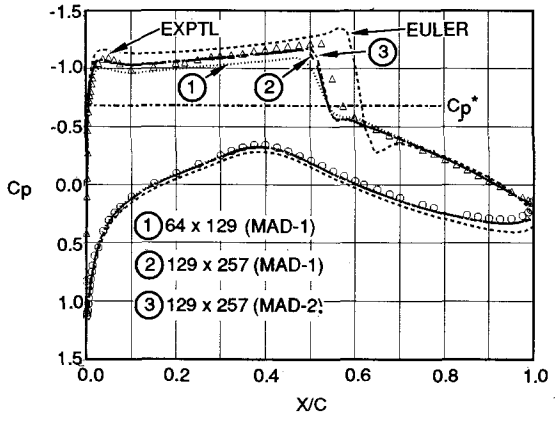

Fig. 3 Correlation of computed and measured surface pressures for RAE 2822 airfoil, $M_\infty = 0.725$, $\alpha = 2.4^o$, $Re = 6.5 \times 10^6$ (AGARD Case 6)

Table 2 Correlation for RAE 2822 Airfoil (AGARD Test Case 6)

	C_l	C_d
Experimental	0.743	0.0127
Euler(64 x 161)	0.874	0.0109
RANS (64 x 161)	0.704	0.0165
RANS (129 x 257)	0.746	0.014

Case 10 This is one of the most difficult cases since there is strong shock-induced boundary-layer separation. For that reason it was chosen to investigate the effectiveness of four turbulence models. The wind-tunnel test parameters are $M_\infty = 0.75$, $\alpha = 3.19^o$ (uncorrected), and $Re_c = 6.2 \times 10^6$. The corrected angle of attack of 2.80^o was used here. Laminar to turbulent transition was tripped in the experiment at x/c = 0.03, but the entire airfoil was considered turbulent in the computations. Thin-layer RANS computations were performed on a six-zone 129 x 257 C grid with sufficient clustering to produce the nondimensional wall coordinate y^+ to be less than unity in the cells adjacent to the solid surface.

Correlation of computed and measured surface pressure coefficient is presented in Figure 4. The Euler computations are included to show the inadequacy of an inviscid computation to accurately model this flow in that the shock location is too far aft and the shock strength is too large. The Baldwin-Lomax turbulence model provides some improvement, but the shock location is still poorly predicted. The RNG and the Johnson-King turbulence models yield much better predictions of the shock location but overpredict the pressure aft of the shock. The Johnson-King predictions are slightly better than those of the RNG predictions. The Chien k-ε turbulence model provides a solution intermediate between the Baldwin-Lomax and Johnson-King models in terms of shock location.

The computed and measured skin friction coefficient on the upper surface is also shown in Figure 4. The Baldwin-Lomax model predicts a separation point too far downstream. The RNG model predicts the separation point well but the flow does not reattach as in the experiment. The Johnson-King model results in good separation point prediction and a skin friction coefficient in the reattached flow of the correct magnitude. The Chien model gives a separation point too far downstream, and then the flow abruptly reattaches to predict excessively high skin friction values. A finer grid near the solid surface may provide better skin friction values in the reattachment region. Further investigations are continuing.

Lockheed-AFOSR Wing C.-- This wing, shown in Figure 5, is characteristic of a transonic maneuver fighter. It has a leading-edge sweep of 45^o, aspect ratio of 2.6, and a taper ratio of 0.3. It was analyzed at its design conditions of $M_\infty = 0.85$ and $\alpha = 5^o$ using several grids. Sensitivity of computations to dissipation and grid density using C-H type grids were previously reported by Raj [8,9]. Inviscid as well as viscous solutions on a C-O grid, which better models the tip region, are presented here.

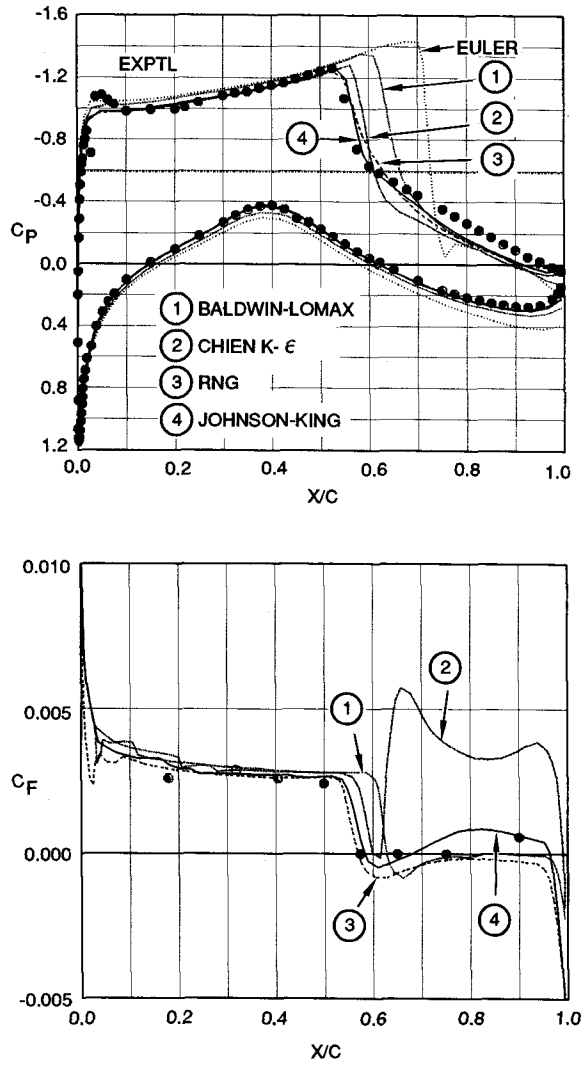

Fig. 4 Correlation of computed and measured surface pressures and skin-friction coefficients for RAE 2822 airfoil, $M_\infty = 0.75$, $\alpha = 2.8^o$, Re = 6.2×10^6 (AGARD Case 10)

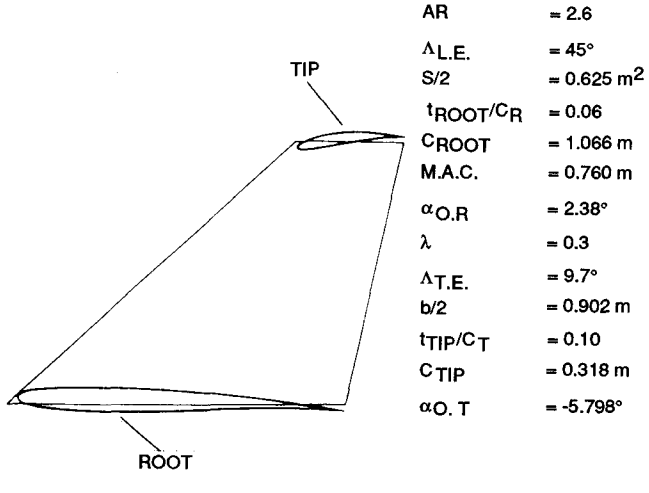

Fig. 5 Lockheed-AFOSR Wing C geometric features

To evaluate the sensitivity of Euler solutions to grid refinement, solutions on a coarse grid with 112,875 nodes (129 nodes in the wrap around direction, 35 nodes between the root and the tip, and 25 in the normal direction) were compared with those on refined grids. The coarse grid was divided into an inner and an outer zone, each having a 13 x 129 x 35 grid. The effect of increasing the number of nodes in the normal direction from 13 to 25 or in the spanwise direction from 35 to 49 was minimal. However, increasing the number of nodes in the wrap around direction from 129 to 257 dramatically changed the solution, especially on the outboard stations, as shown in Figure 6. Note that only the inner zone was refined leading to Class 2 type interfaces for some grids but no detrimental effects were noted. To the contrary, retaining coarser grid in the outer zone afforded a computationally efficient means of evaluating the grid refinement effects.

The effect of numerical dissipation was investigated by comparing computed surface pressures (not included here) corresponding to the SAD, MAD, and FAD schemes. For this study, the values of VIS-2 and VIS-4 were set at 0.5 and 1.5 respectively. The SAD scheme was found to be too dissipative as evidenced by a forward location of shocks compared to the solutions of the other two schemes. The MAD-2 scheme was not as robust and required increasing VIS-4 to 2.0 to obtain a converged solution.

For viscous analysis, a 7-zone C-O grid with a total of 458,745 nodes (51 x 257 x 35) was used. The thin-layer RANS equations were solved in six inner zones and the Euler equations in one outer zone. All interfaces were Class 1 type. The free-stream conditions were: $M_\infty = 0.85$, $\alpha = 5^o$, and Re_{mac} = 10 million (based on mean aerodynamic chord). In Figure 7, the computed solutions are compared with two sets of measured data, one from a large-scale test [32] and the other from a small-scale test [33]. Note that the Reynolds number and the Mach number are the same for the two test data, but the angles of attack are different. The large-scale test data corresponds to $\alpha = 5^o$ and the small-scale test data to 5.9^o; the measured lift coefficients and the leading-edge pressure peaks match for these values. The viscous solutions show better agreement with the measured data than the inviscid solutions, particularly for the outboard stations. However, discrepancies remain which may be due to the coarseness of the grid and/or inadequacy of the Baldwin-Lomax turbulence model to simulate localized flow separation on the outer parts of the wing demonstrated by experimental data [32]. Further analysis using other models as well as finer grids is needed to isolate the source of discrepancy.

Canard-Wing-Body.— TEAM analysis of the canard-wing-body configuration, shown in Figure 8, demonstrates the ability of the code to model transonic flow about a relatively complex configuration and also illustrates its ability to simulate canard-wing interaction. Raj et al. [34] presented correlation of computed solutions at $M_\infty = 0.9$ and $\alpha = 4^o$ for this configuration, with canard in position 1 and wing in position 6 (see Figure 8), using a five-zone grid of H-H topology. Each of the zones had 168 planes between the upstream and the downstream boundaries, and 34 planes between the plane of symmetry and the outboard side boundary. The canard upper and lower surfaces were each defined by a 34 x 13 grid (34 nodes chordwise and 13 spanwise). The wing upper and lower surfaces were each defined by a 38 x 22 grid. Analysis of

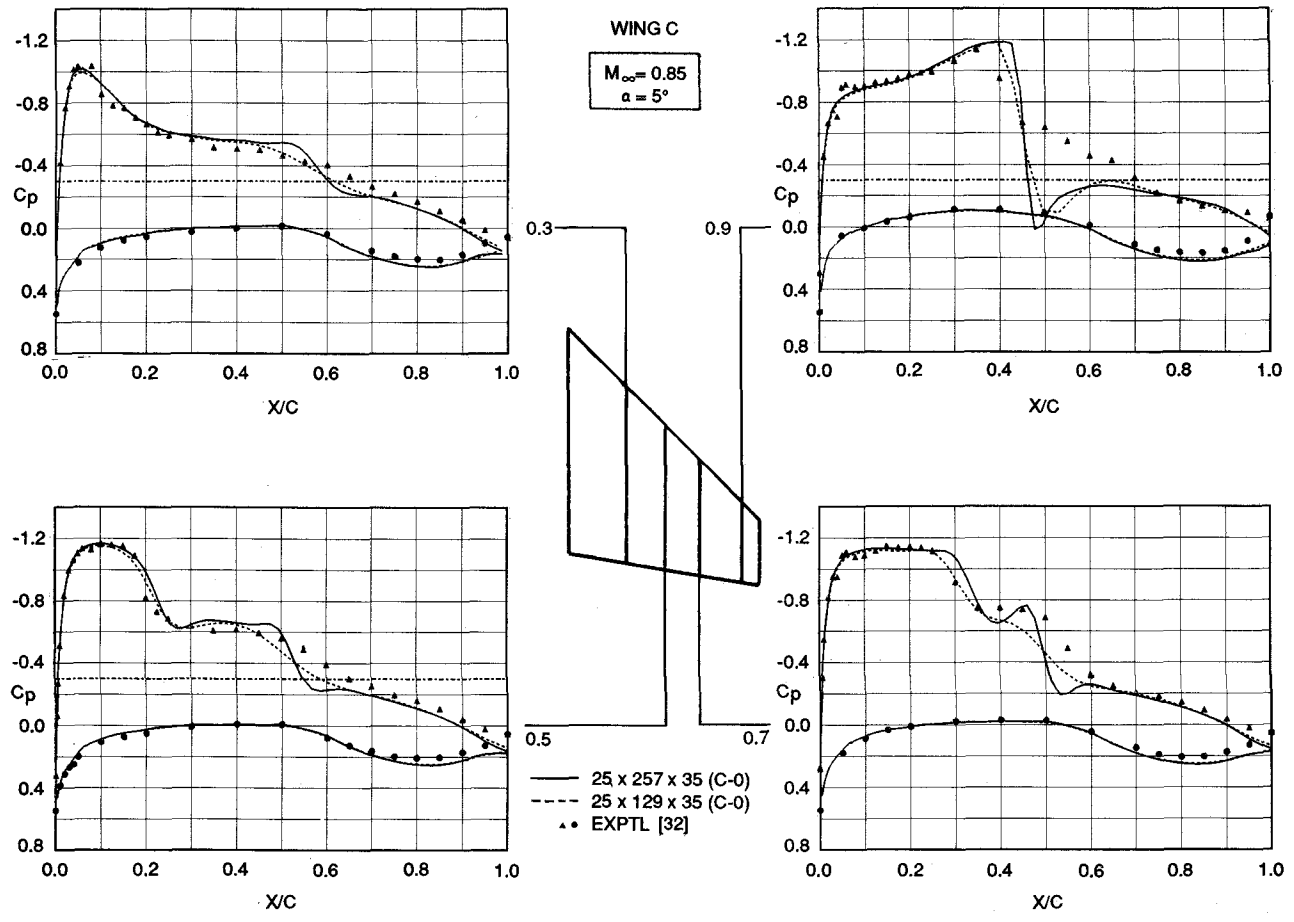

Fig. 6 Sensitivity of TEAM Euler computations to grid density for Wing C, $M_\infty = 0.85$, $\alpha = 5^o$

the canard-off configuration was done using the same number of points.

In order to examine trade-offs between accuracy and efficiency resulting from reduced grid densities in the outer regions of the flow field, further analysis was carried out on three 36-zone grids: (1) a 521,220-node grid with Class 1 interfaces obtained by subdividing the five zones of the baseline grid; (2) a 457,980-node grid with Class 2 interfaces obtained by deleting grid lines along one parametric direction in selected outer zones; and (3) a 400,028-node grid with Class 2 interface obtained by deleting grid lines in two parametric directions in selected outer zones. A comparison of all computed solutions showed excellent agreement for forces and moments as well as surface pressures indicating negligible effect of using coarse grids in the outer zones on accuracy while improving computational efficiency through reductions in computing time proportional to the reductions in the total number of nodes.

Computed lift and drag coefficients correlated well with the measured data of Stewart et al. [35]. In Figure 9, surface pressures corresponding to the MAD-1 and FAD schemes are compared with each other and experimental data at four stations on the wing for the $\alpha = 4^o$ case. Good overall agreement is found with the exception of the shock location. The computed shock is located approximately 10 percent aft of the measured one. Such a discrepancy is, however, typical of inviscid simulations of flows exhibiting significant shock/boundary-layer interaction. For the present case, effects of such an interaction are seen in the measured data but not simulated in the TEAM computations carried out to date.

ANC Fighter Configuration.-- The ANC fighter configuration, shown in Figure 10, represents the first complete aircraft geometry analyzed using the TEAM and TRANSAM codes. This configuration features close-coupled canards mounted on the outboard side of podded engine nacelles which are separated from the fuselage by straked-wing sections. The results demonstrate the ability of the TEAM code to compute flow field around a complete aircraft configuration.

It was analyzed at $M_\infty = 1.19$ and $\alpha = 0.42$, 2.6, 4.85, and 7.11 degrees using a 27-zone H-H type grid with 378,464 cells. The grid generation process is described in detail by Olling and Mani [13]. At the inlet face of the nacelle, the MFR value was set at 0.75. At the exhaust face of the nacelle, the NPR value was set at 7.6. Viscous effects on the wing were simulated for the 4.85^o and 7.11^o cases at $Re_{mac} = 5.77$ million. Thin-layer RANS equations were solved only in zones surrounding the wing. Of course, the grids were appropriately clustered. The Baldwin-Lomax turbulence model was used for the results presented here.

Correlations of inviscid Euler and measured [36] C_L vs α and C_L vs C_D data are presented in Figure 11. In Figure 12, the chordwise surface C_p distributions at two wing stations are shown for both Euler and thin-layer RANS analyses at α =

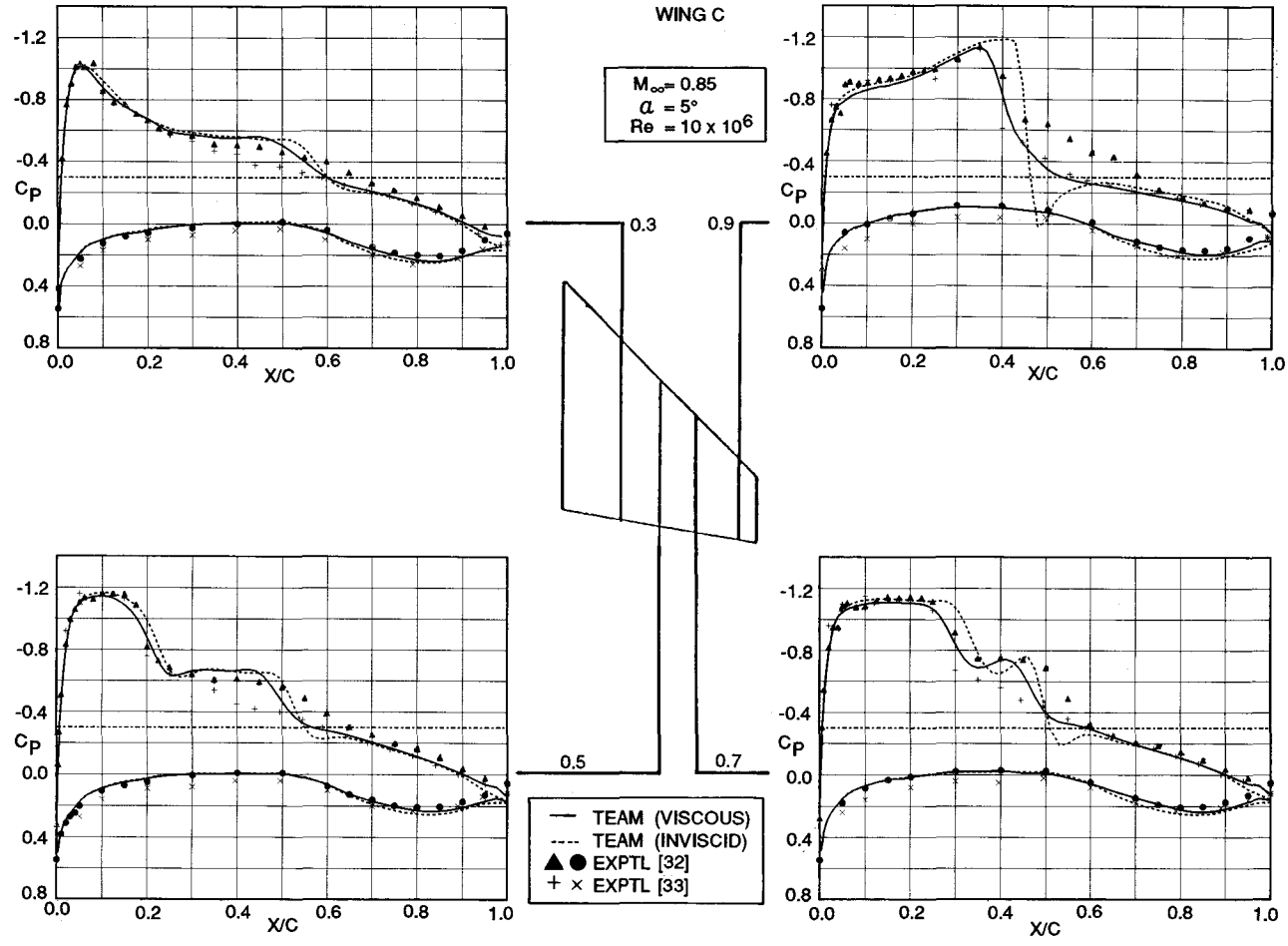

Fig. 7 Correlation of TEAM inviscid and viscous solutions and experimental data for Wing C, M_∞ = 0.85, α = 5°, Re = 10x10^6

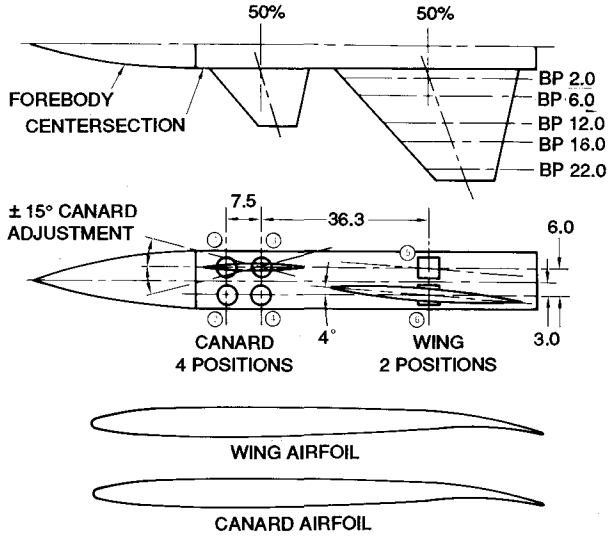

Fig. 8 Canard-wing-body configuration geometric features

7.11°. For the inboard station, the computed values could be correlated with the available measured data of Zilz et al. [36]. These solutions indicate that the viscous effects are not significant on the wing.

IV. Concluding Remarks

During the 1980s, considerable progress was made in developing computational techniques to solve the Euler and Reynolds-averaged Navier-Stokes equations about complex configurations. However, the full range of capabilities of the computational methods is not known. A thorough evaluation of the capabilities requires (1) conducting sensitivity studies to investigate the effect of various computational parameters, such as, grid density, turbulence models, treatment of boundary conditions, etc., on the solutions and (2) correlating computed solutions with experimental data to determine the accuracy of the computed solutions. Only then can the methods be considered validated for routine aerodynamic analysis. Of course, the enormity and the importance of the evaluation task should not be underestimated. With that in mind, this paper should be considered as a small contribution towards a better understanding of the capabilities and limitations of the computational solutions of the Euler and Navier-Stokes equations.

The computational methods considered here, namely, TEAM and TRANSAM, afford a cost-effective means of obtaining steady-state solutions to the Euler and RANS equations. The codes accommodate patched multizone structured grids of arbitrary topologies and thereby facilitate analysis of

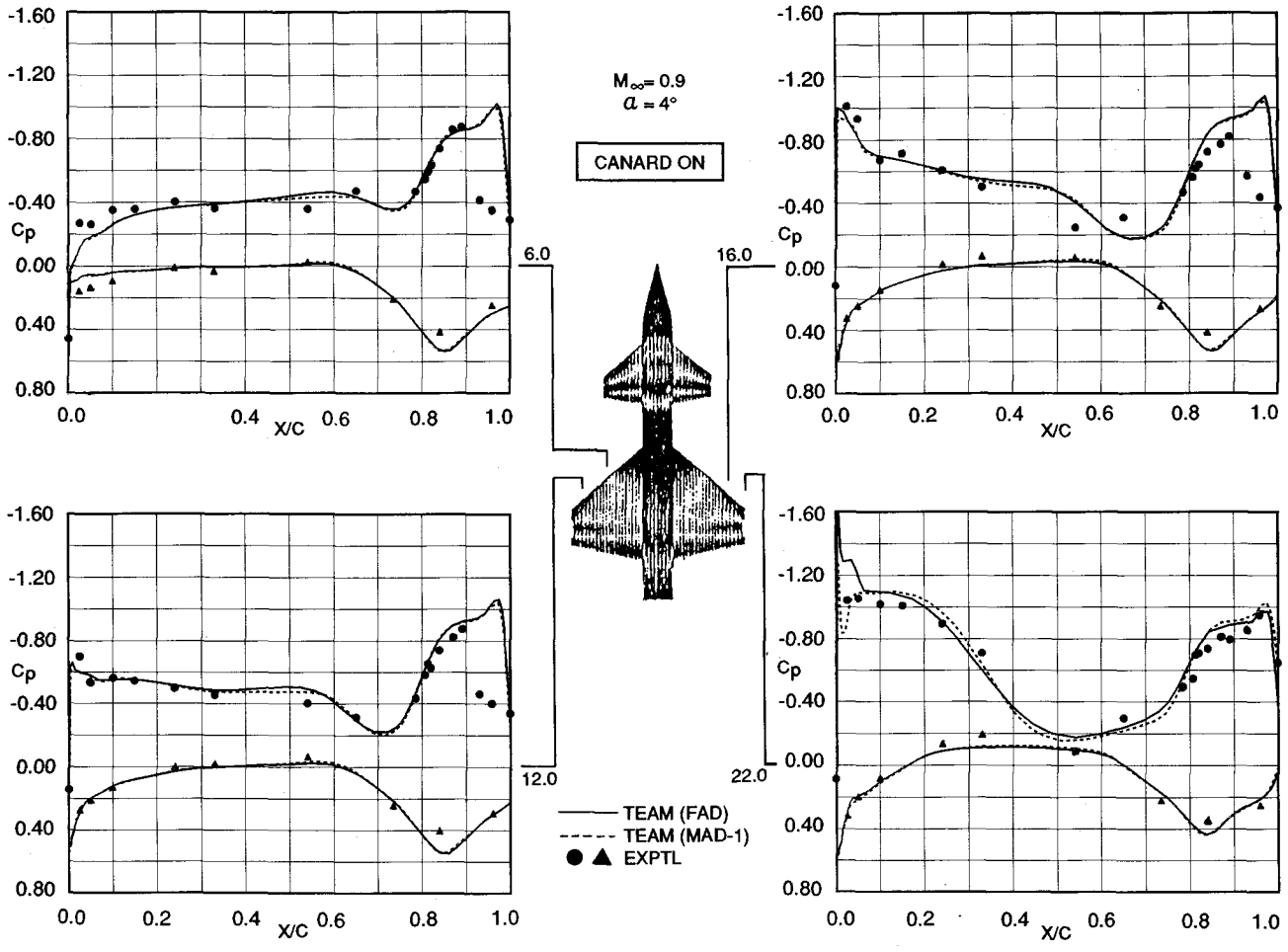

Fig. 9 Sensitivity of TEAM Euler computations to numerical dissipation for canard-wing-body configuration, M_∞ = 0.9, α = 4°

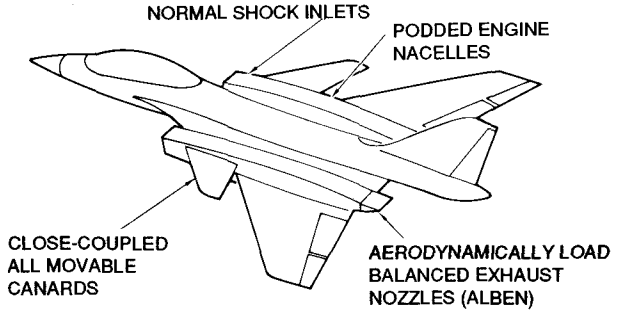

Fig. 10 Supersonic ANC fighter configuration

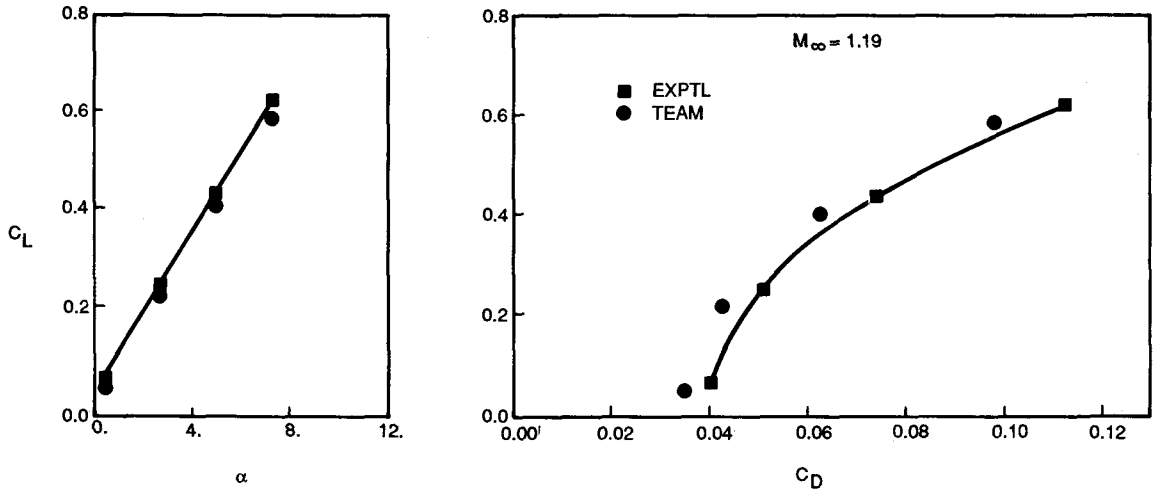

Fig. 11 TEAM Euler computations and measured values of lift and drag coefficients for ANC fighter, $M_\infty = 1.19$

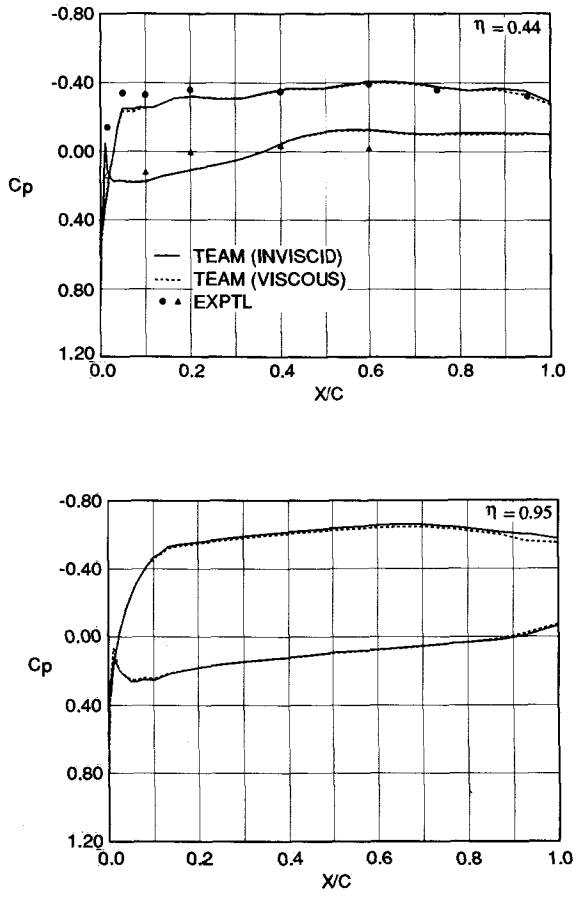

Fig. 12 Comparisons of TEAM inviscid and viscous surface pressures at two wing stations for ANC fighter, $M_\infty = 1.19$, $\alpha = 7.11^o$, $Re = 5.77 \times 10^6$

complex configurations. This was demonstrated in this paper by the solutions for five test cases ranging from 2-D airfoils to a complete aircraft. The ability to generate suitable grids about aircraft configurations in a timely manner is the key to using the codes effectively. Grid generation continues to be a challenging task and is considered a pacing item for effectively using the advanced computational methods.

The results presented in this paper demonstrated the ability of the TEAM and TRANSAM codes to simulate a variety of flows. Correlations with experimental data illustrated the sensitivity of the solutions to turbulence modeling, particularly for separated flows. Also, effects of grid density and numerical dissipation were investigated. With similar ongoing investigations, it is only a matter of time when the codes become even more effective for practical aerodynamic analysis.

Acknowledgements

This investigation was partly supported by an Independent Research and Development project of Lockheed Aeronautical Systems Company, Burbank. The authors acknowledge the invaluable assistance of Mr. J. S. Sikora in developing the codes. Thanks are due to Mr. J. S. Reaser for his assistance in the ANC analysis.

References

1. Miranda, L. R., Elliott, R. D., and Baker, W. M., "A Generalized Vortex Lattice Method for Subsonic and Supersonic Flow Applications," NASA CR 2865, December 1977.

2. Magnus, A. E., Ehlers, F. E., and Epton, M. A., "PANAIR - A Computer Program for Predicting Subsonic or Supersonic Linear Potential Flow About Arbitrary Configurations Using a Higher-Order Panel Method," NASA CR 3251, April 1980.

3. Youngren, H. H., Bouchard, E. E., Coopersmith, R. M., and Miranda, L. R., "Comparison of Panel Method Formulations and Its Influence on the Development of QUADPAN, an Advanced Low Order Panel Method," AIAA Paper 83-1827, July 1983.

4. Johnston, C. E., Youngren, H. H., and Sikora, J. S., "Engineering Applications of an Advanced Low-Order Panel Method," SAE Paper 851793, October 1985.

5. Boppe, C. W., "Aerodynamic Analysis for Aircraft with Nacelles, Pylons, and Winglets," NASA CR 4066, April 1987.

6. Caughey, D. A. and Jameson, A., "Progress in Finite-volume Calculations for Wing-Fuselage Combinations," AIAA Journal, Vol. 18, No. 11, November 1980, pp 1281-1288.

7. Raj, P., "A Multigrid Method for Transonic Wing Analysis and Design," Journal of Aircraft, Vol. 21, No. 2, February 1984, pp 143-150.

8. Raj, P., "Recent Developments in the Computational Solutions of Euler Equations (Invited Paper)," Third International Congress of Fluid Mechanics, Cairo, Egypt, January 2-4, 1990.

9. Raj, P., "An Euler Code for Nonlinear Aerodynamic Analysis: Assessment of Capabilities," Advanced Aerospace Aerodynamics, SAE SP-757, October 1988, pp 215-230.

10. Rai, M. M. and Moin, P., "Direct Simulation of Turbulent Flow Using Finite-Difference Schemes," AIAA 89-0369, January 1989.

11. Holst, T. L., "Viscous Transonic Airfoil Workshop Compendium of Results," AIAA Paper 87-1460, 1987.

12. Flores, J. and Chaderjian, N. M., "The Numerical Simulation of Transonic Separated Flow About the Complete F-16A," AIAA Paper 88-2506, June 1988.

13. Olling, C. R. and Mani, K. K., "Navier-Stokes and Euler Computations of the Flow Field Around a Complete Aircraft," Advanced Aerospace Aerodynamics, SAE SP-757, October 1988, pp 231-242.

14. Huband, G., Rizzetta, D., and Shang, J., "The Numerical Simulation of the Navier-Stokes Equations for an F-16 Configuration," AIAA 88-2507-CP, June 1988.

15. Thompson, J. F. and Steger, J. L., "Three-dimensional Grid Generation for Complex Configurations--Recent Progress," (Ed. Yoshihara, H.), AGARD-AG-309, March 1988.

16. Sengupta, S. et al. (Ed.), "Numerical Grid Generation in Computational Fluid Mechanics," Pineridge Press, 1988.

17. Lakshminarayana, B., "Turbulence Modeling for Complex Shear Flows," AIAA Journal, Vol. 24, No. 12, December 1986, pp 1900-1917.

18. Raj, P., Olling, C. R., Sikora, J. S., Keen, J. M., Singer, S. W., Brennan, J. E., "Three-dimensional Euler/Navier-Stokes Aerodynamic Method (TEAM), Volume I: Computational Method and Verification," AFWAL-TR-87-3074 (Revised), June 1989.

19. Jameson, A., Schmidt, W., and Turkel, E., "Numerical Solution of the Euler Equations by Finite-Volume Methods Using Runge-Kutta Time-Stepping Schemes," AIAA Paper 81-1259, 1981.

20. Baldwin, B. S. and Lomax, H., "Thin Layer Approximation and Algebraic Model for Separated Turbulent Flows," AIAA Paper No. 78-275, 1978.

21. Martinelli, L. and Yakhot, V., "RNG-Based Turbulence Transport Approximations With Applications to Transonic Flows", AIAA Paper 89-1950-CP, 1989.

22. Johnson, D. A. and King, L. S., "A Mathematically Simple Turbulence Closure Model for Attached and Separated Turbulent Boundary Layers", AIAA Journal, Vol. 23, pp. 1684-1692, 1985.

23. Chien, K.-Y., "Predictions of Channel and Boundary-Layer Flows with a Low-Reynolds-Number Turbulence Model", AIAA Journal, Vol. 20, pp. 33-38, 1982.

24. Degani, D. and Schiff, L. B., "Computation of Supersonic Viscous Flows Around Pointed Bodies at Large Incidence", AIAA Paper 83-0034, 1983.

25. Abid, R. and Johnson, D. A., "Effects of Turbulence Models on the Prediction of Transonic Wing Flows", SAE Paper 892224, 1989.

26. Jayaram, M. and Jameson, A., "Multigrid Solution of the Navier-Stokes Equations for Flow Over Wings," AIAA Paper 88-0705, January 1988.

27. Jameson, A., "A Nonoscillatory Shock Capturing Scheme Using Flux Limited Dissipation," MAE Report 1653, Princeton University, Princeton, New Jersey, 1983.

28. Gnoffo, P. A., McCandless, R. S., and Yee, H. C., "Enhancements to Program LAURA for Computation of Three-Dimensional Hypersonic Flow," AIAA Paper 87-0280, 25th Aerospace Sciences Meeting, Reno, Nevada, January 12-15, 1987.

29. Viviand, H., "Numerical Solutions of Two-Dimensional Reference Test Cases," Chapter 6, AGARD-AR-211, May 1985.

30. Raj, P., "TEAM: A Three-dimensional Euler Aerodynamic Method," AIAA Professional Study Series, Euler Solvers Workshop, Monterey, California, August 20-21, 1987.

31. Cook, P. H., McDonald, M. A., and Firmin, M. C. P., "Aerofoil RAE 2822 - Pressure Distributions, and Boundary Layer and Wake Measurements", AGARD Advisory Report No. 138, Paper A6, 1979.

32. Keener, E. R., "Pressure-Distribution Measurements on a Transonic Low-Aspect Ratio Wing," NASA TM 86683, September 1985.

33. Hinson, B. L. and Burdges, K. P., "Acquisition and Application of Transonic Wing and Far-Field Test Data for Three-Dimensional Computational Method Evaluation," AFOSR-TR-80-0421, March 1980.

34. Raj, P., Keen, J. M., and Singer, S. W., "Applications of an Euler Aerodynamic Method to Free-Vortex Flow Simulation," AIAA Paper 88-2517-CP, June 1988.

35. Stewart, V. R., "Evaluation of a Propulsive Wing/Canard Concept at Subsonic and Supersonic Speeds," Rockwell International Report NR82H-85, Volume I, August 1983.

36. Zilz, D. E., "Propulsion and Airframe Aerodynamic Interactions of Supersonic V/STOL Configurations," Vols. I and II, NASA CR-177343, 1985.

37. Radespiel, R., Rossow, C., and Swanson, R.C., "An Efficient Cell-Vertex Multigrid Scheme for the Three-Dimensional Navier-Stokes Equations," AIAA 89-1953-CP, June 1989.

38. Swanson, R. C. and Turkel, E., "Artificial Dissipation and Central Difference Schemes for the Euler and Navier-Stokes Equations," AIAA 87-1107-CP, June 1987.

39. Eriksson, L., "Transfinite Mesh Generation and Computer-Aided Analysis of Mesh Effects," Doctoral Dissertation, Uppsala University, Uppsala, Sweden, March 1984.

Appendix A

Numerical Dissipation

The mathematical formulations of the numerical dissipation schemes are briefly described in this Appendix. The vector of flow variables is defined as $w = [\rho, \rho u_m, \rho E]^T$ where ρ denotes density; u_m are velocity components with subscript $m = 1,2,3$ denoting the component in Cartesian X, Y, or Z direction respectively; and E is total energy. The static pressure is denoted by p.

Standard and Modified Adaptive Dissipation.-- These schemes are based on a blending of first and third differences in each of the three parametric index directions. The i-direction dissipative flux at the interface between two cells identified by (i,j,k) and (i+1,j,k) sets of indices is considered here. Expressions for other index directions can be analogously written.

$$D_{i+1/2,j,k} = \varepsilon_2 \, d_{i+1/2,j,k} - \varepsilon_4 \, e_{i+1/2,j,k} \qquad (A\text{-}1)$$

where

$$d_{i+1/2,j,k} = \phi \; \lambda^i_{i+1/2,j,k} \left(w_{i+1,j,k} - w_{i,j,k} \right)$$

$$e_{i+1/2,j,k} = \varepsilon_4 \left(d_{i+1/2,j,k} - 2 d_{i,j+1/2,k} + d_{i,j-1/2,k} \right)$$

Note that the terms d and e are formally proportional to the first and third differences of flow variables respectively. The scaling factor ϕ is varied to construct different dissipation schemes. In the present work, the following formulations have been considered.

$\phi = 1 + r_{ji} + r_{ki}$ SAD scheme [18]

$\phi = 1 + \max(r^{\alpha}_{ji}, r^{\alpha}_{ki})$ MAD-1 scheme [37]

$\phi = 1$ MAD-2 scheme [38]

Here α is typically 0.5, and

$$r_{ji} = \lambda^j_{i+1/2,j,k} \; / \; \lambda^i_{i+1/2,j,k}$$

$$r_{ki} = \lambda^k_{i+1/2,j,k} \; / \; \lambda^i_{i+1/2,j,k}$$

$$\lambda^i_{i+1/2,j,k} = \frac{1}{2} \left[\lambda^i_{i+1,j,k} + \lambda^i_{i,j,k} \right]$$

Here, λ^i, λ^j, λ^k are the spectral radii of the flux-Jacobian matrices in the i, j, and k directions respectively.

The coefficients of the first- and third-difference terms in Equation (A-1) are constructed as follows:

$$\varepsilon_2 = \kappa_0 \, \bar{\nu}_{i+1/2,j,k} \quad \text{and} \quad \varepsilon_4 = \max(0, \kappa_1 - \varepsilon_2)$$

where

$$\bar{\nu}_{i+1/2,j,k} = \max \left(\nu_{i+2,j,k}, \nu_{i+1,j,k}, \nu_{i,j,k}, \nu_{i-1,j,k} \right)$$

and $$\nu_{i,j,k} = \left| \frac{p_{i+1,j,k} - 2\, p_{i,j,k} + p_{i-1,j,k}}{p_{i+1,j,k} + 2\, p_{i,j,k} + p_{i-1,j,k}} \right|$$

For MAD schemes, ε_2 is redefined as

$$\varepsilon_2 = \min (1/2, \kappa_0 \bar{\nu}_{i+1/2,j,k})$$

A user-specified coefficient, VIS-2, defines κ_0 and another user-input coefficient, VIS-4, divided by 64, defines κ_1.

Boundary Formulation Since the present algorithm considers only one image cell, the dissipative terms need to be constructed differently for the boundary faces than those for the interior. For the boundary face at i = 3/2 (see Figure A-1 below), three options have been considered as discussed below.

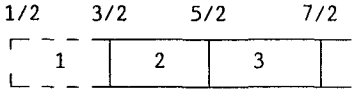

Figure A-1

Option 1: Following Eriksson [39], the first and third differences are set to zero at i = 3/2 and the third difference at i = 5/2 is reduced to a second difference, i.e.,

$$d_{3/2,j,k} \equiv 0 \quad \text{and} \quad e_{3/2,j,k} \equiv 0$$

$$e_{5/2,j,k} \equiv d_{7/2,j,k} - d_{5/2,j,k}$$

This is formally equivalent to using a zeroth-order extrapolation of flow variables to define values in the image cell at i = 1.

Option 2: In this option, the following assumption is made about the first differences near the boundary faces.

$$d_{1/2,j,k} \equiv d_{3/2,j,k} \equiv d_{5/2,j,k}$$

This is equivalent to a linear two-point extrapolation of the flow variables to define flow variables in i = 0 and i = 1 image cells. (Note that only i = 1 image cell is considered in the present algorithm). This results in the third difference term going to zero at the boundary and reducing to a second difference at i = 5/2 just like for Option 1.

Option 3: Using the following assumption for first differences at i = 1/2 face,

$$d_{1/2,j,k} = 2\, d_{3/2,j,k} - d_{5/2,j,k}$$

results in the third difference at the boundary (i = 3/2) going to zero; the values at i = 5/2 are not affected. This is equivalent to a three-point extrapolation of flow variables to define the flow variables in the i = 0 image cell.

Flux-Limited Adaptive Dissipation.— For this scheme, the dissipative flux term at a cell face is expressed as:

$$D_{i+1/2,j,k} = B(d_{i+3/2,j,k},\, d_{i+1/2,j,k}) - 2\, d_{i+1/2,j,k} + B(d_{i+1/2,j,k}, d_{i-1/2,j,k}) \quad \text{(A-2)}$$

where the limiter operator, B, with arguments a and b is defined as

$$B(a,b) = (s(a) + s(b)) \min (|a|, |b|)$$

$$s(a) = \begin{cases} 1/2 & , a \geq 0 \\ -1/2 & , a < 0 \end{cases}$$

The first differences are defined as in Eq. (A-1) except that the scaling factor is now given by:

$$\phi = \min (1/2, \kappa_0 + \kappa_1 \bar{\nu}_{i+1/2,j,k})$$

The values of κ_0 and κ_1 are specified through user-specified VIS-2 and VIS-4 parameters respectively. As pointed out by Jameson [27], if ϕ is set to 1/2, the scheme is TVD but excessively dissipative.

Near the boundaries, options similar to the ones for SAD and MAD schemes were incorporated. However, the best performance is achieved by setting D (see Eq. (A-2)) to zero at the boundary face.